Original Research

Influence of Thermal Environment Conditions on Mechanical Properties of MEX Printed 17-4 PH Stainless Steel

Bruno Schubert [*], David Hochmann

Biomechatronics Research Laboratory, FH Münster University of Applied Sciences, Steinfurt, Germany; E-Mails: bruno.schubert@fh-muenster.de; david.hochmann@fh-muenster.de

* **Correspondence:** Bruno Schubert; E-Mail: bruno.schubert@fh-muenster.de

Academic Editor: Seyed Ghaffar

Special Issue: Additive Manufacturing Technology in Construction

Abstract

This study investigates the influence of thermal environmental conditions during printing and their effects on the mechanical properties of material extrusion (MEX) 3D-printed 17-4 PH stainless steel. Various ambient temperatures and cooling behaviors were used during the printing process of the tensile specimens. Following DIN EN ISO 50125 and DIN EN ISO 6892, the study analyzes tensile strength, elongation and yield strength. The results demonstrate that the thermal environmental conditions affect both tensile and yield strength. Subsequent analysis indicates that changes in the mechanical properties result from alterations in the microstructure of the material due to the thermal environment. The elongation of printed specimens shows consistent behavior under varying thermal environmental conditions. In conclusion, careful consideration of the thermal environment is necessary for controlling and optimizing the mechanical properties of MEX-printed 17-4 PH stainless steel.

Keywords

Stainless steel 17-4 PH; metal 3D printing; additive manufacturing; material extrusion; mechanical properties; influence of thermal conditions

1. Introduction

Additive manufacturing (AM) has revolutionized material fabrication, allowing for complex structures with unprecedented design freedom [1]. Material extrusion (MEX) is a widely used method for plastic component fabrication due to its versatility and cost-effectiveness [2, 3]. The materials available constantly evolve, with new options emerging on the market. The range of MEX-capable materials includes flexible and fiber-reinforced materials for high-stressed applications [4]. In some cases, even higher mechanical properties are required, which is where metal 3D printing comes into play. Metal 3D printing is often associated with Laser Powder Bed Fusion (LPBF), in which a potent laser fuses metal powders together to form solid structures. The layered structure is typically formed by applying a thin layer of powder after the laser fusing is complete. Once the printing process is complete, the excess powder must be removed from the printed objects before being cut from the build plate. Finally, any support structures required for large overhangs can be removed. This processing step involves a variety of machines and tools, which can add significant cost to the entire production chain [5, 6].

Metal MEX printing is an alternative to the LPBF process. The key features of the technology are the MEX material and processing steps. The filament used combines metal powder, composite plastics and binder material for printability [5]. The filament can be loaded and printed on most standard MEX-based printers. After printing, the composite and binder material must be removed in a two-step catalytic and thermal process, leaving only the bare fused metal part. This fabrication process chain requires less tooling than the LPBF process and can be achieved at lower investment costs [5]. The European market offers some suppliers of this type of material and technology, including BASF 3D Printing Solution GmbH, PT+A GmbH, Desktop Metal, and Markforged, among others. Markforged and Desktop Metal also offer a complete supply chain in a closed system, namely Metal X and Studio System 2. The advantage and disadvantage of these closed systems is that the possibility of varying parameters is severely limited. For this study, BASF's metal MEX printing process was selected due to its open system approach, which allows for outsourcing post-processing steps to a service provider from BASF, thereby reducing the overall cost and effort [6].

BASF currently offers two types of stainless steel: 316L and 17-4 PH [7]. Of these, 17-4 PH is particularly important for improving the reliability and performance of MEX-printed metallic structures due to its widespread use in industries where high strength, corrosion resistance, and thermal stability are essential. The MEX process has demonstrated remarkable capabilities in producing complex geometries with this material [5].

Quality control and assurance are crucial in advanced manufacturing, especially in high-stress applications [8]. The increasing use of 3D printing in such demanding scenarios makes it essential to ensure the integrity and reliability of printed parts. The 3D printing process requires careful attention to ensure that the final product meets high mechanical performance, durability, and precision standards. While quality management systems and ISO standards are available to control product quality in conventional manufacturing, there is a lack of practical standards and recommendations for quality management in 3D printing [9]. Despite this, meeting the requirements depends on selecting the correct printing parameters. These parameters include factors such as layer height, line width, infill density, part orientation and structure, and many others that have already been researched [6, 10]. However, it is noteworthy that external factors such as

ambient temperature and thermal conditions during the printing process are equally important but have not been extensively studied.

Therefore, the current study comprehensively investigates the complex relationships between thermal environmental conditions and the resulting mechanical properties of 17-4 PH stainless steel. The objective is to examine the relationship between ambient temperatures and cooling behaviors while printing tensile specimens. The critical mechanical properties such as tensile strength, elongation and yield strength are analyzed according to the standards DIN EN ISO 50125 and DIN EN ISO 6892 [11, 12]. By systematically varying these thermal conditions, this study aims to determine the quantitative effects on the mechanical characteristics and the underlying mechanisms at the microstructural level.

2. Materials and Fabrication of the MEX Specimens

A spool of Ultrafuse 17-4 PH filament purchased from BASF was used to print the tensile specimens. The composite material consists of 88 wt% 17-4 PH stainless steel particles and 12 wt% polyoxymethylene (POM) polymer binder mixture [13]. According to BASF, this material can be printed on any standard desktop MEX-based printer [14].

The CreatBot F430 desktop MEX printer was used to print the samples in this investigation. The enclosed core-xy MEX printer has a dual extruder print head. One hotends has a 0.4 mm hardened steel nozzle for printing abrasive filaments, including Ultrafuse 17-4 PH. A standard bronze nozzle would be worn down by the stainless steel particles in the filament, causing print errors.

BASF has published a design guideline for their Ultrafuse filaments to outline printing parameters and other recommendations for the printing process [15]. Table 1 shows the printing parameters used for the tensile specimen. A brim with a thin layer of Magigoo Metal glue stick was applied to the glass printing surface to improve adhesion to the print bed.

Table 1 Printing parameters for the Ultrafuse 17-4 PH tensile specimen [15].

Parameter	Value
Nozzle size	0.4 mm
Extrusion width	0.4 mm
Layer height	0.2 mm
Outlines	4
Infill	100% Rectilinear
Nozzle temperature	245°C
Bed temperature	100°C
Print speed	30 mm/s
Cooling	None

The tensile specimens in this study meet the specifications of DIN EN ISO 50125 [11]. Flat specimens were printed with the identifier DIN 50125 - E 4 × 10 × 35 for better printability. The dimensions are illustrated in Figure 1 and Table 2. To reduce statistical fluctuations, three tensile specimens were printed simultaneously. The samples were printed lying flat side by side with sufficient space between them. G-code was generated using Creatware V7.0.2. Software and applied to all prints to ensure consistency.
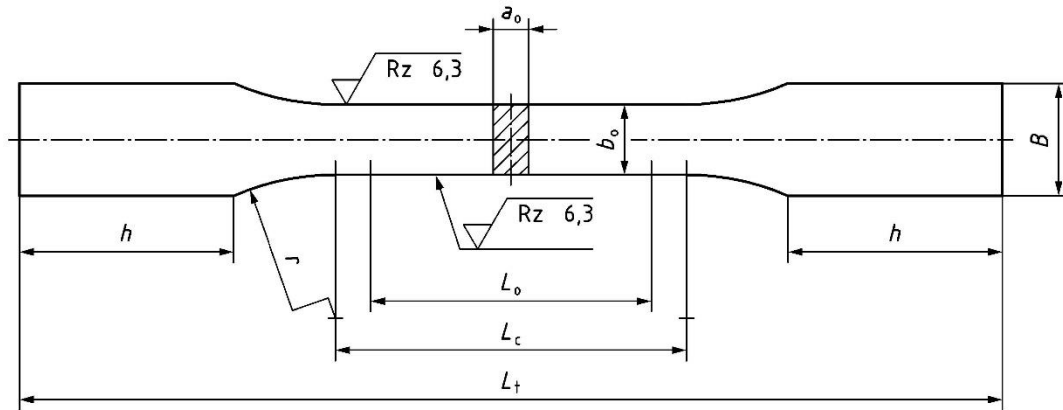
**Figure 1** Sample geometry according to DIN 50125 for Type E, flat bar with machined parallel length [11].

Table 2 Dimensions for tensile test specimen geometry DIN 50125 - E $4 \times 10 \times 35$ in [mm].

a_O	b_y	L_O	B	r	h	L_c	L_t
4	10	35	15	12	30	45	120

After printing, the sample was transferred to Elnik Systems GmbH, a BASF-licensed service provider, for the catalytic debinding and sintering steps. Catalytic debonding is a thermochemical process that removes part of the binder matrix by exposing the printed parts to gaseous nitric acid (HNO_3 >98%) in a nitrogen atmosphere at a temperature of 120°C. The duration of this step depends on the thickness of the printed part, and it is completed when a minimum debinding loss of 10.5% is achieved. The part is then referred to as the brown part. The remaining polymer binder serves as the necessary stabilizing element for the sintering process.

In the sintering step, the brown part undergoes a gradual thermal process in which the remaining binder is burned off and the 17-4-PH stainless steel particles are fused into a solid metal part. The thermal process is divided into two phases and occurs in a hydrogen atmosphere to prevent oxidation and other detrimental processes. In the first phase, the part is heated from ambient temperature to 600°C at a rate of 5 K/min and held for one hour. The sample is then heated to 1300°C at the same rate and held for three hours for the second phase, after which the furnace is cooled to room temperature [16].

The process-related removal of the binder resulted in shrinkage of the parts. To achieve the desired geometry, the green parts must be oversized per the guidelines set forth by BASF. The shrinkage behavior in the x-y plane is approximately 20%, while in the z-direction, it is approximately 24% [15]. Calibration cubes containing different geometric test shapes (see Figure 2) were printed in a preliminary internal test of the material. These cubes demonstrated the potential for variation in the measured values, dependent on the shape of the printed part. Concerning the bone-shaped tensile specimens, our findings indicate that a scaling factor of approximately 18% in the xy-plane and 21% in the z-direction was sufficient.
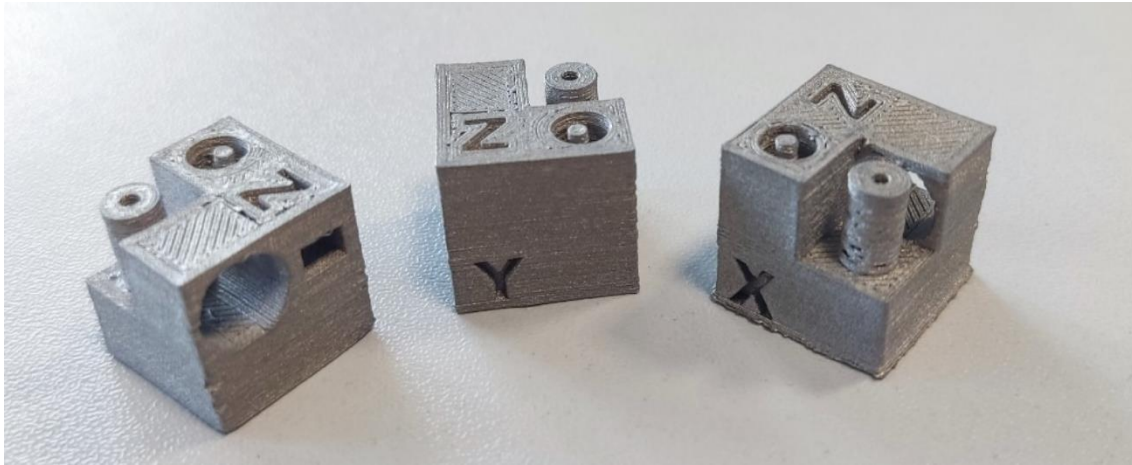
Figure 2 Calibration cubes used for shrinkage and oversizing tests.

The scaling factors were applied using the Creatware slicing software. The measured dimensions of each sample, both before and after sintering, are shown in Table 3. The values of r, L_c and L_0 were not measured due to impracticality. Shrinkage was calculated from the difference between the pre- and post-sintering values, as shown in Table 3. For each axis, the shrinkage factors in the X and Y directions were combined to determine the actual values, resulting in:

- X-axis shrinkage factor: 16.94 ± 0.33%
- Y-axis shrinkage factor: 16.04 ± 0.27%
- Z-axis shrinkage factor: 19.51 ± 1.00%

Despite the differences between the expected and actual shrinkage factors, all components meet the minimum requirements of DIN EN ISO 50125 [11].

Table 3 Measured dimension of the 3D-printed specimen before and after sintering.

Specimen No.	1-1	1-2	1-3	2-1	2-2	2-3	3-1	3-2	3-3	4-1	4-2	4-3
before sintering [mm]												
a_0	5.03	4.86	4.88	4.86	4.92	4.92	4.91	4.95	4.98	4.94	4.95	4.98
b_0	12.25	12.16	12.19	12.17	12.16	12.19	12.04	12.02	12.00	12.15	12.11	12.08
B	18.06	18.01	18.03	18.08	18.03	18.10	18.02	17.87	17.82	18.19	18.18	18.07
h	35.22	35.35	35.28	35.29	35.52	35.69	35.44	35.38	35.79	35.58	36.18	35.47
L_t	141.18	141.31	141.17	141.04	141.26	141.07	140.93	140.93	140.83	141.18	141.83	140.91
after sintering [mm]												
a_0	4.01	3.92	4.00	3.99	3.95	4.00	3.97	3.99	3.97	3.88	3.97	3.98
b_0	10.09	10.04	10.05	10.05	9.87	10.4	9.95	9.90	9.89	10.04	9.90	9.95
B	15.27	14.98	15.02	15.15	15.06	15.14	15.12	15.04	15.08	15.24	15.25	15.06
h	29.54	29.71	29.85	29.78	29.54	29.97	29.66	29.88	29.97	29.84	29.89	29.98
L_t	118.33	118.20	118.37	118.47	118.64	118.26	118.51	118.4	118.46	118.92	118.70	118.70
Shrinkage [%]												
a_0	20.28	19.34	18.03	17.90	19.72	18.70	19.14	19.39	20.28	21.46	19.80	20.08
b_0	17.63	17.43	17.56	17.42	18.83	17.64	17.36	17.64	17.58	17.37	18.25	17.63
B	15.45	16.82	16.69	16.21	16.47	16.35	16.09	15.84	15.38	16.22	16.12	16.66
h	16.13	15.95	15.39	15.61	16.84	16.03	16.31	15.55	16.26	16.13	17.39	15.48
L_t	16.19	16.35	16.15	16.00	16.01	16.17	15.91	15.99	15.88	15.77	15.71	15.76

3. Experimental Methods

The general thermal printing parameters, including the nozzle and bed temperature, were not varied or investigated in this study. The study instead concentrated on the impact of thermal environmental conditions. Two primary factors were analyzed to determine their effect on the mechanical properties of the printed parts. First, the ambient temperature during the printing process was investigated. Therefore, the actively heated build chamber of the CreatBot printer, which can continuously vary the chamber temperature up to 70°C, was used. Due to the secondary heating effects of the printhead and bed, it was decided to investigate only the upper and lower limits of the ambient air temperature. The maximum ambient temperature was found to be 117°C, considering both the active heating and the temperature emitted by the printhead and the print bed. In the absence of additional heating, the minimum ambient temperature was observed to be 58°C, considering the temperature emitted by the components above. Second, the effect of cooling conditions after the print was completed was analyzed. To achieve a controllable and consistent cooling behavior, three 40 mm DC fans were installed on one of the side covers of the printer, which were activated after the print was completed. This allowed two cooling scenarios to be studied: one with slow passive cooling to room temperature without the fans activated and one with fast cooling enabled by the activated fans. The combination of these two primary factors results in four environmental scenarios to investigate:

- minimum chamber temperature without additional cooling fans enabled (condition 1),
- minimum chamber temperature with additional cooling fans enabled (condition 2),
- maximum chamber temperature with additional cooling fans enabled (condition 3),
- maximum chamber temperature without additional cooling fans enabled (condition 4),

Two PT100 temperature sensors are positioned inside the build chamber to ensure comparable thermal conditions and monitor its temperature. The sensors are strategically placed: one above the print bed and head in the center of the chamber and the other below the print bed, as shown in Figure 3. The sensor signal is processed and logged by the HBM QuantumX amplifier. A Python script is used to generate and evaluate the data obtained from the sensors.
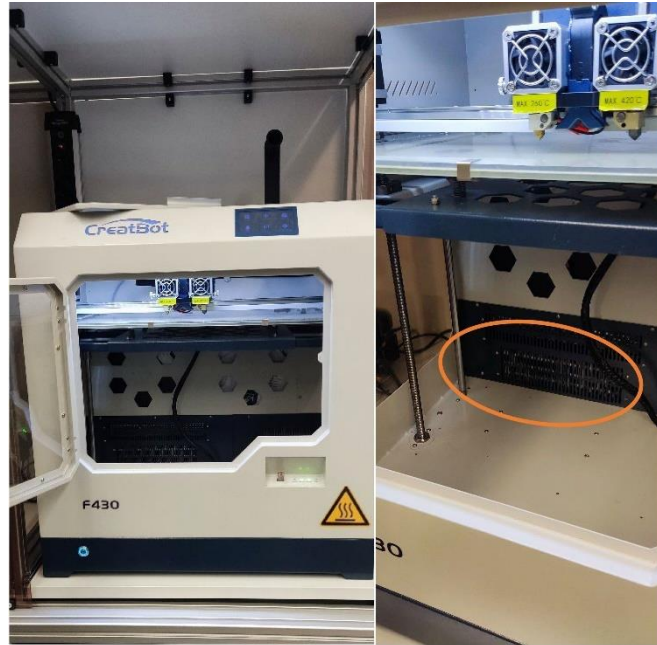
Figure 3 Outside and inside view of the CreatBot F430, with the chamber heating highlighted on the right.

The cooling process is complete when both PT100 sensors reach ambient room temperature. It was expected that the temperature graphs for the slow cooling condition without additional fans would show a longer time to get the room temperature of around 23°C than those with fans.

The variance in cooling time due to the presence of additional fans resulted in a time saving of approximately 2 hours and 13 minutes between conditions 1 and 2. For conditions 3 and 4, the additional fans resulted in a time saving of approximately 3 hours, while the effect of active heating during the printing process - which resulted in a higher ambient temperature at the start of the cooling phase - resulted in a time difference of about 1 hour between conditions 1 and 4, and about 30 minutes between conditions 2 and 3.

Figure 4 shows the temperature curves for the different cooling conditions as measured by two PT100 temperature sensors placed inside the printer. Measurement began after the print was completed. The graphs demonstrate that the sensor above the print bed (red) recorded higher temperatures than the sensor below the print bed (blue) when the heat chamber is inactive. Conversely, the temperatures were reversed when the heating is active during the printing process. This change in the curves corresponds to the location of the heating element in the lower left corner of the build chamber, as shown in Figure 3.
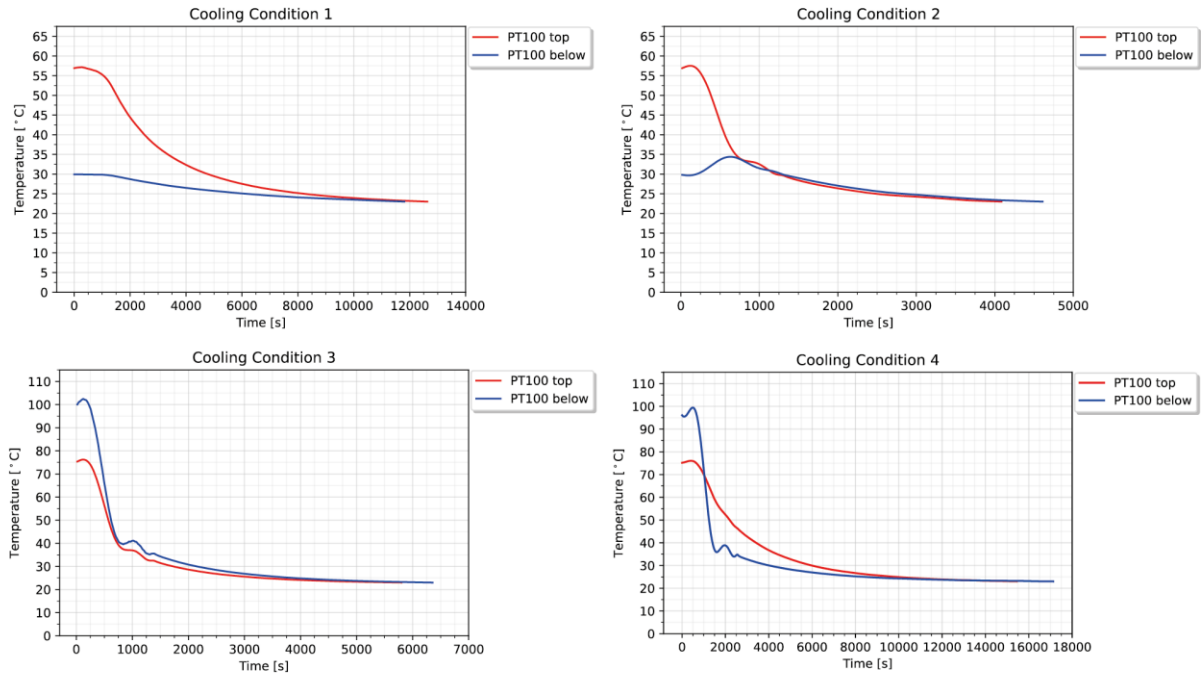
Figure 4 Temperature curves for cooling conditions 1-4 measured by PT100 sensor placed inside the 3D-printer.

4. Tensile Testing

The 3D-printed specimens were subjected to tensile testing using a Zwick AllroundLine static material testing machine. The machine had a 100 kN load cell and a makroXtens II extensometer. Hydraulic specimen grips were used to withstand the high test forces. A pressure of approximately 330 bar was applied to the holders. These holders ensure precise and consistent placement of each specimen see Figure 5. The resulting measurements included tensile strength [MPa], yield strength [MPa], and elongation [%]. Test parameters were applied according to DIN EN ISO 6892. Three samples were printed and tested for each environmental condition to reduce statistical variation.
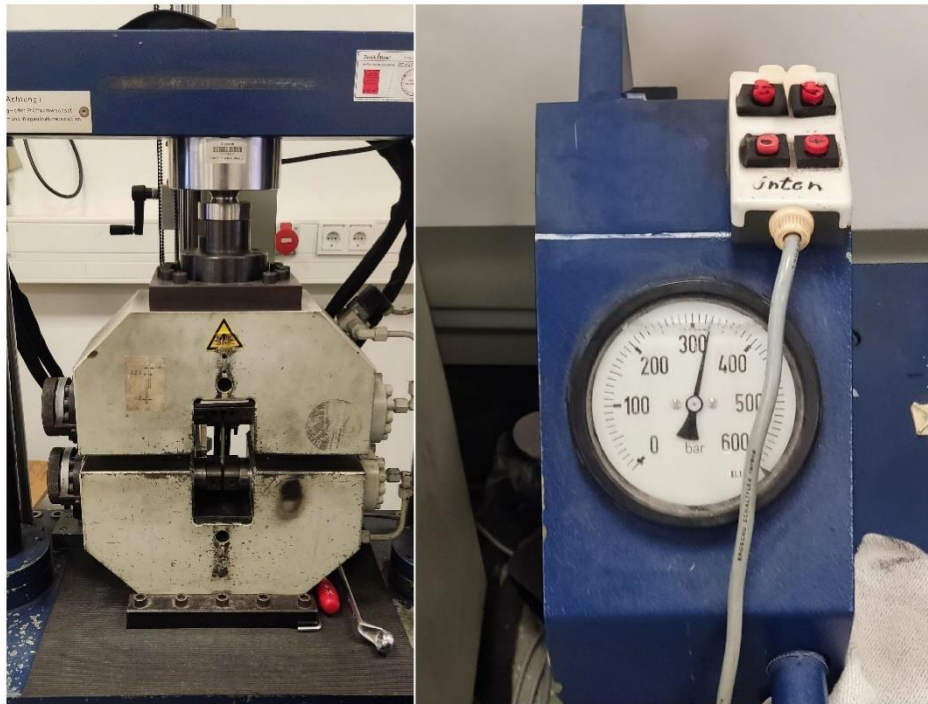
Figure 5 Zwick AllroundLine static material testing machine (left) and hydraulic control of the sample holders (right).
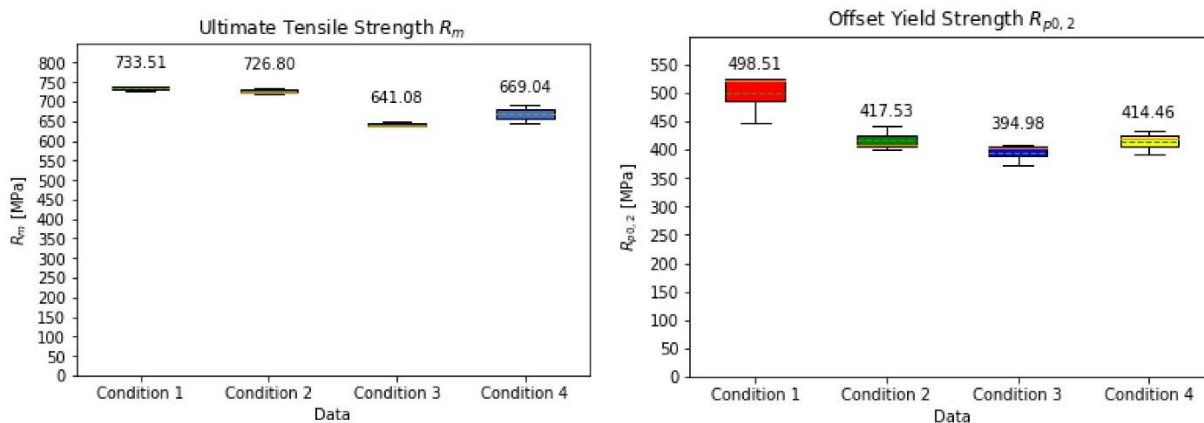
5. Results

This section presents the results of the tensile tests performed on the printed samples, focusing on the variation in mechanical behavior resulting from different environmental conditions during the printing process. Figure 6 shows the stress-strain diagram for all samples. The first digit of the specimen identifier indicates the thermal condition of the specimen, while the second digit identifies the badge specimen.
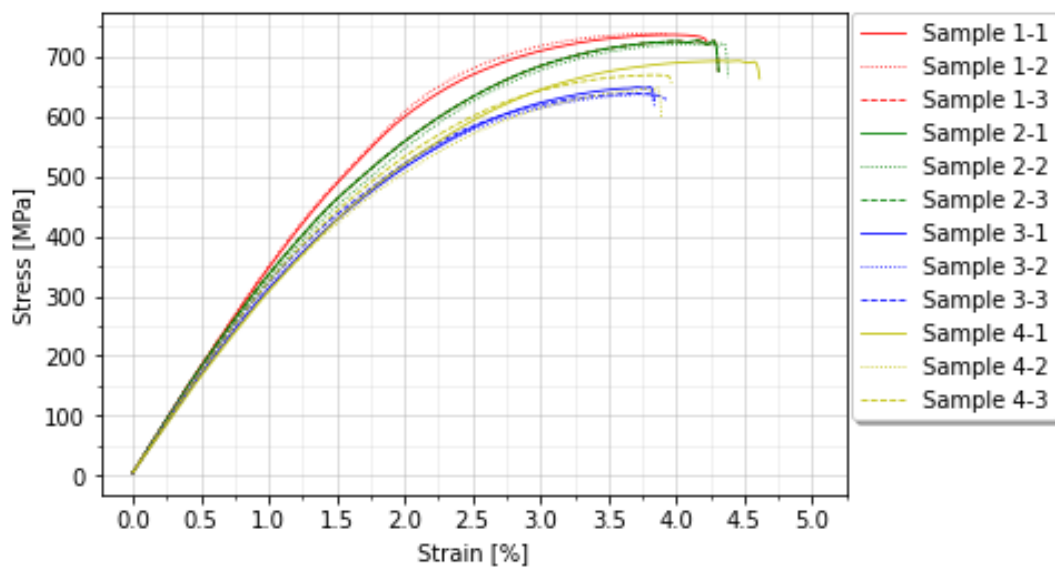
Figure 6 Stress-strain diagram for all specimens.

Figure 6 illustrates that the stress-strain curves have a consistent gradient across all specimens tested. Each specimen reaches a strain range between 3.75% and 4.75% before failure. The maximum stress reached before failure varies between the conditions. Conditions 1 and 2 reach similar ranges, while the results for conditions 3 and 4 are significantly lower. Overall, the condition 3 specimens produced the weakest results in both elongation and strength. The measured ultimate tensile strength and the offset yield strength separately in Figure 7.


Figure 7 Tensile test results of all specimens for each environmental printing condition.

The samples from condition 1 achieved the highest values for ultimate tensile strength (733.51 ± 5.86 MPa) and offset yield strength (498.51 ± 35.91 MPa). Condition 2 achieved a similar ultimate tensile strength (726.80 ± 6.00 MPa) but lower offset yield strength (417.53 ± 17.72 MPa) than condition 1. Condition 3, as noted earlier in the stress-strain curves, produced the weakest values for both ultimate tensile strength (641.08 ± 19.43 MPa) and offset yield strength (394.98 ± 15.43 MPa). The values produced by condition 4 are slightly higher than those of condition 3 but still lower than those of condition 1 and 2. When comparing the offset yield strength, conditions 2, 3, and 4 achieved similar values, with only condition 1 producing significantly higher values. Comparing the best and worst results, there is a difference of about 92.43 MPa in ultimate tensile strength and about 103.53 MPa in offset yield strength between conditions 1 and 3, which is a critical difference in mechanical properties.

The comparison of tensile strength data concerning environmental conditions shows that the influence of chamber temperature results in a difference of more than 4 times greater than that of cooling behavior. For example, when combining condition 1 with 2 and 3 with 4 for the same chamber temperature, the mean difference is approximately 75.09 MPa. When the difference in the cooling behavior is combined with the differences between 1 with 2 and 3 with 4 separately, the mean difference is approximately 17.33 MPa.

This study also analyzed elongation behavior by tensile testing. Figure 7 shows the results for elongation at break and percentage elongation after fracture for each condition. The graph shows no significant differences in elongation at break or percentage elongation after fracture between the different conditions. In contrast to the tensile test, condition 1 did not achieve the highest values for either elongation at break or the percentage elongation after fracture. Condition 2 achieved the highest overall values, but the differences from the other means were not found to be significant. It is important to note that condition 3 produced the weakest results and the most consistent values,

with a standard deviation of approximately 0.042% for elongation at break and 0.066% for percentage elongation after fracture. The values are more variable for all other conditions, as shown in Figure 8.
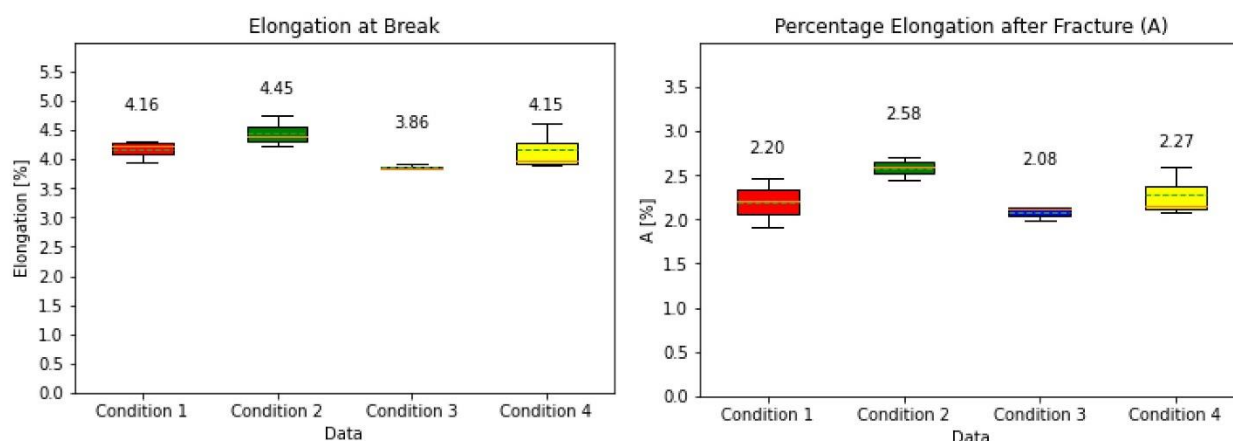
Figure 8 Elongation at break (left) and percentage elongation after fracture (right).

Table 4 shows a comparison between the data provided by BASF in the data sheet and the current study. However, the data sheet does not provide information on the percentage elongation after fracture. All mechanical properties were significantly lower under all conditions. Comparing the best results of this study with the datasheet values, we see that there is a difference of approximately 147 MPa in ultimate tensile strength. This translates to approximately 17% less load ability than the reference from BASF. The difference in offset yield strength is similar, with absolute values of roughly 182 MPa, which results in over 27% less strength than BASF. Comparing the worst results of the study shows a difference of approximately 239 MPa or 27% in ultimate tensile strength and approximately 286 MPa or over 42% in offset yield strength.

Table 4 Tensile test results compared to the BASF data sheet [16].

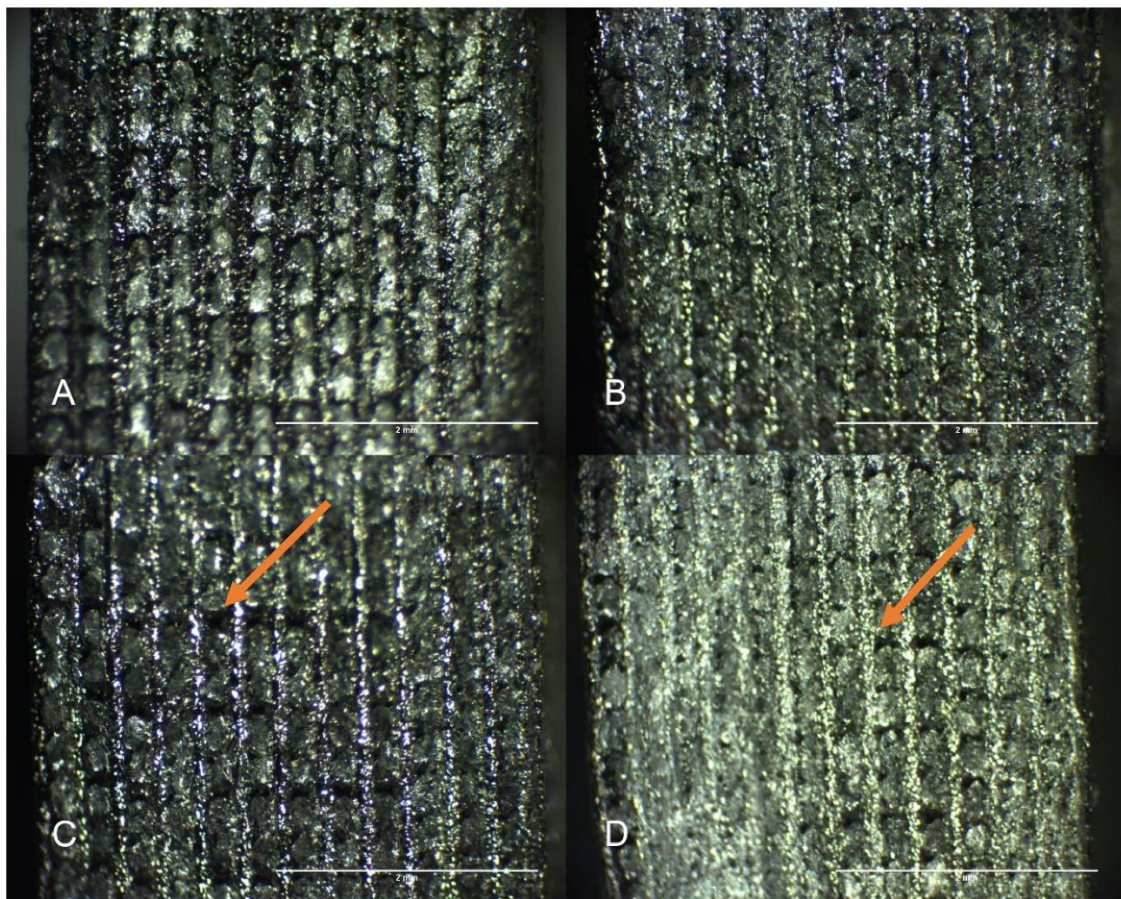|	Condition 1	Condition 2	Condition 3	Condition 4	BASF
Ultimate Tensile Strength [MPa]	733.51 ± 5.86	726.80 ± 6.00	641.08 ± 5.09	669.04 ± 19.43	880
Offset Yield Strength [MPa]	498.51 ± 35.91	417.53 ± 17.72	394.98 ± 15.43	414.46 ± 17.09	680
Elongation at Break [%]	4.16 ± 0.15	4.45 ± 0.21	3.86 ± 0.04	4.15 ± 0.32	5.8
Percentage Elongation after Fracture [%]	2.20 ± 0.22	2.58 ± 0.10	2.08 ± 0.06	2.27 ± 0.22	-

According to the BASF data sheet, the same DIN standard was applied to their tensile test [16]. The current study and the BASF test differ only in the shape of the specimen. BASF used a smaller specimen with the identifier E2×6×20 according to DIN 50125. However, this cannot be the sole reason for the significant difference in mechanical properties [11]. Since a service provider licensed by BASF performed the post-processing steps, they should be applied similarly. The only differences that cannot be verified are the printing parameters and environmental conditions used by BASF.

These were not described in the data sheet and may differ from the settings used in this study. However, it can be assumed that BASF follows its guidelines, which were also applied in this study.

The mechanical properties of specimens obtained from different environmental conditions exhibit significant variability, indicating that the thermal environment may induce defects in the material layering during the printing process, which would reduce the overall part density. To test this hypothesis, a comparative analysis of fracture surfaces was conducted to determine how different temperatures during printing might affect the microstructure and, consequently, the mechanical performance. The specimens exhibiting the most significant property variability relative to their manufacturing environment were subjected to fractographic examination.

Images of the fractured edges were obtained using an Olympus BH3-MJL reflected light microscope in order to identify any irregularities or defects that could be attributed to thermal effects during layer deposition. Figure 9 shows a visual representation of the microscopic analysis. The images demonstrate significant variations in fracture morphology across specimens produced under diverse thermal conditions.

Figure 9 Microscopic images of the fracture edges of one specimen from each condition, scale bar 2 mm (A: condition 1, B: condition 2, C: condition 3, D: condition 4).

It is important to note that no surface treatments were employed before microscopy, thereby ensuring an accurate observation of the fracture characteristics induced by the printing conditions alone. This method provides a direct, unaltered view of the internal structure at the failure site, offering insights into defects, including porosity, crack propagation paths, and layer separation.

The images depicted in Figure 9 clearly indicate variances in defect size and distribution among samples, suggesting a correlation between environmental temperature during printing and density irregularities within the material. The images 9 shows distinct black dots in images C and D that are not present in image A and are less present in image B. This indicates that there are variances in defect size and distribution among samples. It also suggests a correlation between environmental temperature during printing and density irregularities within the material. These defects manifest in an irregular pattern and vary in size. They also act as weak spots in the cross-section of the sample, contributing to the observed poor mechanical properties. Figure 10 presents a more detailed view of the fractured edge of the condition 3 specimen.
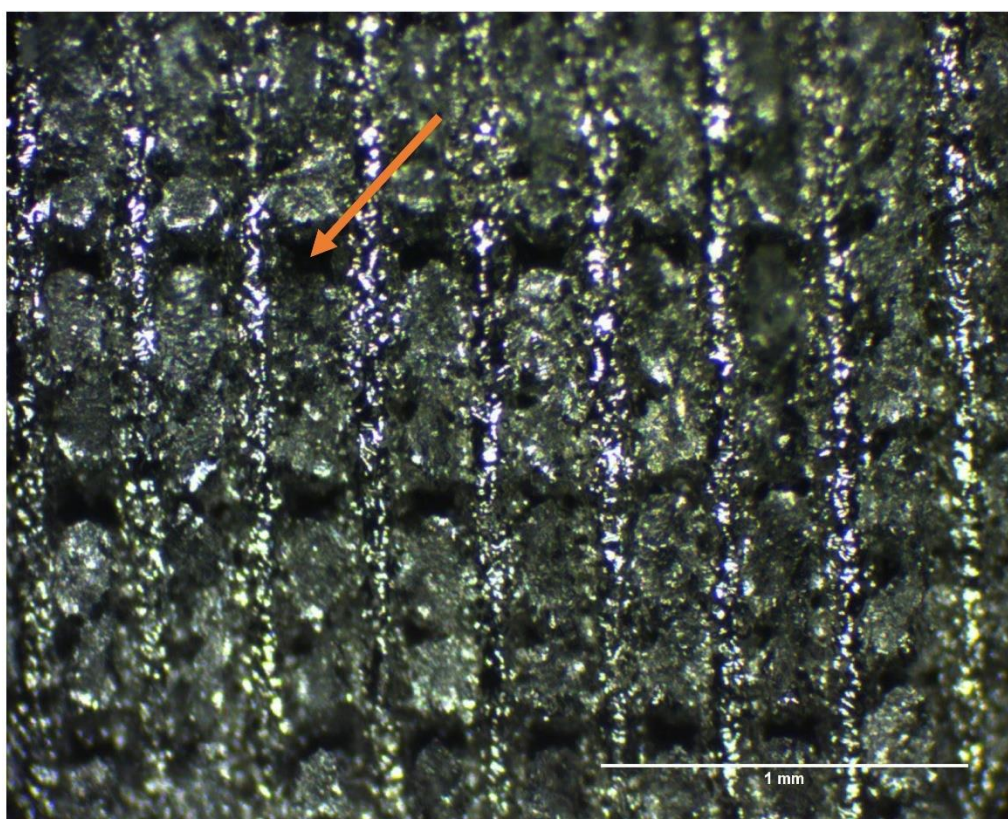
Figure 10 Enlarged image of the fracture edge of specimen 2 from condition 3 with an indicator showing a defect.

Since the debinding and sintering processes were conducted uniformly for all samples, the lower part density was observed during the printing of the green parts. The degree of part density variation could be gauged according to the number and dimensions of material defects. Without suitable equipment, it was impossible to ascertain the sample density in this investigation. However, microscopic images indicated that environmental conditions influenced the printing process, thereby leading to pronounced variations in the mechanical properties of the samples. Further research is necessary to identify the optimal printing conditions for producing highly stressed metal MEX printed parts.

6. Discussion

In order to compensate for the shrinkage during the sintering process, the green parts must be printed with an oversized dimension. The oversizing factor utilized in this study differed from the recommendations provided by BASF. Initial tests with the material indicated that shrinkage is dependent on the shape of the printed part and deviates from the provided guidelines. Consequently, the oversizing factor was adjusted to 18% for the x and y directions and 21% for the z direction. Despite these adjustments, the shrinkage measured after sintering exhibited a slight discrepancy from the targeted value. In addition to the geometry of the part, the density of the green part may also contribute to the observed variations in shrinkage. Notwithstanding, the sintered parts satisfied the ISO 50125 requirements.

The investigation into environmental conditions revealed that the ambient temperature during the printing process had a more significant influence on the mechanical properties of printed parts than the cooling conditions. As a consequence of the control loop of the active heating, the temperature exhibited fluctuations of approximately 5°C around the stated maximum. The nonlinear temperature curve rendered the analysis of the cooling behavior challenging, which precluded the calculation of a cooling factor. Furthermore, an anomaly in the temperature curve was observed in cooling conditions 3 and 4, occurring after approximately 16 minutes in condition 3 and 32 minutes in condition 4. This anomaly is likely caused by the automatic shutdown of the printer after printing, as observed in previous prints and test runs.

The analysis of the fracture edge using a reflected light microscope revealed significant defects in the cross-section of the printed part. Black dots were visible under the microscope, indicating areas of missing material. These voids act as local weak spots, leading to low mechanical properties. A microscope with higher magnification is required for a more detailed investigation of these black dots, but unfortunately, one was not available. While a scanning electron microscope (SEM) would be useful for examining the material's microstructural composition, it would not be beneficial for investigating the visible defects under reflected light microscopy. Additionally, SEM equipment was not accessible. For future research, having more advanced optical analysis tools would be beneficial for a detailed examination of the fracture surfaces.

The fractal surface analysis revealed that the overall part density was insufficient. It can be conducted that optimal parameters can be achieved through an iterative process, for example, through the measurement of green parts density. High green part density typically indicates good white part properties, so this process may be an effective method for achieving the desired results. However, selecting an appropriate method for determining green part density is of the utmost importance. Given the inherent porosity of MEX components, the Archimedean principle is not a suitable method for measuring density, as the measuring fluid may infiltrate the component pores, thereby skewing the results [17]. An alternative method would entail measuring the precise volume of the green part through 3D scanning and determining the part's weight to calculate its density. Regrettably, in this study, the parts were neither scanned nor weighed, thus rendering density an inapplicable parameter. It is recommended that future research incorporate green part density as an indicator of print quality.

7. Summary

This study examines the impact of diverse environmental factors and conditions on the mechanical properties of MEX-printed metal components using BASF Ultrafuse 17-4 PH material. The study recorded the thermal conditions and performed tensile tests on each sample. The results demonstrate that the mechanical properties of the parts were influenced by the environmental conditions, resulting in either enhanced or decreased mechanical performance. The environmental conditions significantly influenced the ultimate tensile strength more than the offset yield strength. However, the elongation behavior, remained unaltered. Following the tensile test, the fracture edge cross sections of the most prominent specimen were examined using a reflected light microscope. The microscopic images demonstrated that defects in the material layering occurred in the samples with the lowest mechanical properties, thereby corroborating the hypothesis that the printing process was influenced by the thermal conditions, resulting in a lower part density. Further investigation is necessary to determine the optimal printing parameters and the influence of mechanical properties. Another area for further investigation is the influence of the printing process on fatigue life. This is also a critical aspect, in addition to the static loads investigated in this study. These findings should be particularly considered when employing the MEX metal printing technology for critical applications, such as those in the medical and aerospace fields, or for highly stressed applications, such as construction works and special tooling.

Author Contributions

Bruno Schubert: idea, concept, experiment and writing; David Hochmann: writing, review, and editing.

Competing Interests

The authors have declared that no competing interests exist.

References

1. Alafaghani A, Qattawi A, Alrawi B, Guzman A. Experimental optimization of fused deposition modelling processing parameters: Design for manufacturing approach. Procedia Manuf. 2017; 10: 791-803.
2. Ngo TD, Kashani A, Imbalzano G, Nguyen KT, Hui D. Additive manufacturing (3D printing): A review of materials, methods, applications and challenges. Compos B Eng. 2018; 143: 172-196.
3. Thomas DS, Gilbert SW. Costs and cost effectiveness of additive manufacturing. Gaithersburg, MD: National Institute of Standards and Technology; 2014; NIST special publication 1176.
4. Singh S, Ramakrishna S, Singh R. Material issues in additive manufacturing: A review. J Manuf Process. 2017; 25: 185-200.
5. Gong H, Snelling D, Kardel K, Carrano A. Comparison of stainless steel 316L parts made by FDM- and SLM-based additive manufacturing processes. JOM. 2019; 71: 880-885.
6. Henry TC, Morales MA, Cole DP, Shumeyko CM, Riddick JC. Mechanical behavior of 17-4 PH stainless steel processed by atomic diffusion additive manufacturing. Int J Adv Manuf Technol. 2021; 114: 2103-2114.

7. BASF Forward AM. Metal Filaments [Internet]. Heidelberg, Germany: BASF Forward AM; [cited date 2024 January 29]. Available from: https://forward-am.com/material-portfolio/ultrafuse-filaments-for-fused-filaments-fabrication-fff/metal-filaments/

8. Delgado J, Ciurana J, Rodríguez CA. Influence of process parameters on part quality and mechanical properties for DMLS and SLM with iron-based materials. Int J Adv Manuf Technol. 2012; 60: 601-610.

9. Crowell AM, Cramer SA, Lopez JP, Rashka EK, Reuss RC, Wordsworth VK, et al. Development of a quality assurance tool for additive manufacturing. Proceedings of the 2018 Systems and Information Engineering Design Symposium; 2018 April 27th; Charlottesville, VA, USA. Piscataway Township: IEEE.

10. Godec D, Cano S, Holzer C, Gonzalez-Gutierrez J. Optimization of the 3D printing parameters for tensile properties of specimens produced by fused filament fabrication of 17-4PH stainless steel. Materials. 2020; 13: 774.

11. DIN Media. Testing on metallic–Tensile test pieces. Berlin, Germany: Beuth Verlag GmbH; 2022; DIN 50125:2022-08. doi: 10.31030/3337825.

12. DIN Media. Metallic materials – Tensile testing – Part 1: Method of test at room temperature. Berlin, Germany: Beuth Verlag GmbH; 2020; DIN 6892-1:2020-06. doi: 10.31030/3132591.

13. Pellegrini A, Lavecchia F, Guerra MG, Galantucci LM. Influence of aging treatments on 17–4 PH stainless steel parts realized using material extrusion additive manufacturing technologies. Int J Adv Manuf Technol. 2023; 126: 163-178.

14. BASF Forward AM. Ultrafuse® 17-4 PH—Process Instructions [Internet]. Heidelberg, Germany: BASF Forward AM; 2021 [cited date 2024 January 29]. Available from: https://forward-am.com/wp-content/uploads/2021/01/Process-Instructions-Ultrafuse-17-4-PH.pdf.

15. BASF Forward AM. Ultrafuse® Metal Filaments [Internet]. Heidelberg, Germany: BASF Forward AM; [cited date 2024 January 29]. Available from: https://move.forward-am.com/hubfs/AES%20Documentation/Metal%20Filaments/Ultrafuse_metal_User_Guideline.pdf.

16. BASF Forward AM. Ultrafuse® 17-4 PH [Internet]. Heidelberg, Germany: BASF Forward AM; 2022 [cited date 2024 January 29]. Available from: https://move.forward-am.com/hubfs/AES%20Documentation/Metal%20Filaments/17-4%20PH/TDS/Ultrafuse_17-4PH_TDS_EN_v1.1.pdf.

17. Schumacher C, Moritzer E. Stainless steel parts produced by fused deposition modeling and a sintering process compared to components manufactured in selective laser melting. Macromole Symp. 2021; 395: 2000275.